



**HAL**  
open science

## A novel insight of pBTI degradation in GaN-on-Si E-mode MOSc-HEMT

W. Vandendaele, X. Garros, T. Lorin, E. Morvan, A. Torres, R. Escoffier, Ma  
Jaud, M. Plissonnier, F. Gaillard

► **To cite this version:**

W. Vandendaele, X. Garros, T. Lorin, E. Morvan, A. Torres, et al.. A novel insight of pBTI degradation in GaN-on-Si E-mode MOSc-HEMT. IRPS 2018 - 2018 IEEE International Reliability Physics Symposium, Mar 2018, Burlingame, United States. pp.4B.2-1-4B.2-6, 10.1109/IRPS.2018.8353580 . cea-02185503

**HAL Id: cea-02185503**

**<https://cea.hal.science/cea-02185503v1>**

Submitted on 24 May 2023

**HAL** is a multi-disciplinary open access archive for the deposit and dissemination of scientific research documents, whether they are published or not. The documents may come from teaching and research institutions in France or abroad, or from public or private research centers.

L'archive ouverte pluridisciplinaire **HAL**, est destinée au dépôt et à la diffusion de documents scientifiques de niveau recherche, publiés ou non, émanant des établissements d'enseignement et de recherche français ou étrangers, des laboratoires publics ou privés.

# A novel insight of pBTI degradation in GaN-on-Si E-mode MOSc-HEMT

W. Vandendaele, X. Garros, T. Lorin, E. Morvan, A. Torres, R. Escoffier,  
MA Jaud, M. Plissonnier, F. Gaillard  
CEA-Leti, 17 Avenue des Martyrs  
Grenoble-Alpes University  
Grenoble, 38054, France  
phone: +033 – 438785253, william.vandendaele@cea.fr

**Abstract** — For the first time, ultrafast AC pBTI measurements are applied to GaN on Si E-mode MOSc-HEMT and compared to DC pBTI. Full recess  $\text{Al}_2\text{O}_3/\text{GaN}$  MOS gate is submitted to AC signals with various frequencies, duty factors and stress times. The degradation and relaxation characteristics are then modeled through a RC model combined to a CET map and fitted to experimental data. This map reveals the presence of two trap populations, also observed through  $\Delta V_{\text{th}}$  degradation kinetics. Acceleration factors (gate voltage and temperature) are estimated as well as TTF (Time to Failure) under AC conditions and show an extended lifetime compared to DC stress conditions. Finally dynamic variability is studied and indicates that our devices are ruled by normal distributions.

**Index Terms** — pBTI, GaN on Si, E-mode GaN, AC pBTI, ultrafast pBTI

## I. INTRODUCTION

GaN-on-Si HEMT technology is now considered as a serious candidate for medium power applications (650V rated) [1,2] thanks to a combination of high breakdown field and high electron mobility. In the as grown material, buffer active defects are present in large numbers, inducing electron trapping during electrical stress resulting in the famous current collapse effect. Recently, current collapse free devices [2,3] have been demonstrated by fine tuning GaN on Si epitaxy as well as interfaces passivation. Buffer issues apart, gate instabilities and reliability are a major concern to increase lifetime of the transistors especially when submitted to high reverse bias stress ( $V_{G,\text{OFF}} = 0\text{V}$ ;  $V_{DS,\text{OFF}} > 600\text{V}$ ) and high forward gate voltage ( $V_{G,\text{ON}} > 6\text{V}$ ). Recent TDDDB studies on E-mode p-GaN gate HEMTs [4,5] tend to show an important limitation in maximum ON-state gate voltage to ensure a 10 years lifetime at  $T = 150^\circ\text{C}$  mainly due to a significant increase of the gate current at high  $V_G$  due to the p-GaN gate back to back diodes configuration. MIS gate structure is thus seen as a potential solution to overcome this maximum gate swing limitation. Nevertheless, in this very case, BTI degradation has to be assessed. This latter effect would severely impact the dynamic performance of the transistors over the time. D-mode MIS HEMTs, with either SiN or  $\text{Al}_2\text{O}_3$  gate oxide, have been extensively studied through nBTI [6] and pBTI [7,8,9] studies and has shown a strong  $V_{\text{th}}$  shift related to border traps and oxide bulk traps. An advanced E-mode MOSc-HEMT (MOS-channel-HEMT) configuration [10,11] has recently been introduced on 200mm GaN on Si wafers and submitted to harsh gate conditions aging [12]. So

far only DC BTI measurements have been reported while these transistors are supposed to operate only in AC conditions for ON-state mode. In addition, slow measurements ( $> 1\text{ms}$ ) are generally reported which tend to modify the actual  $V_{\text{th}}$  drift during the stress phase. In this paper we present for the first time a comparison between AC and DC stress combined with ultra-fast pBTI measurements ( $< 10\mu\text{s}$ ) on GaN-on-Si E-mode MOSc-HEMTs embedding an  $\text{Al}_2\text{O}_3$  gate oxide.

## II. DEVICE DESCRIPTION AND EXPERIMENTAL SETUP

### A. Device description

200mm GaN-on-Si wafers were grown using metal organic chemical vapor deposition (MOCVD). A structure consisting of "Transition Layers" is grown directly on a 1mm thick lightly doped ( $\sim 10 \Omega\cdot\text{cm}$ ) p-type Si substrate. A Carbon doped GaN (GaN:C) layer is then grown on top to ensure electrical insulation between the substrate and the top active layer while improving GaN breakdown voltage, and the GaN growth is finished with a thin unintentionally doped GaN layer (GaN:UID) which forms the channel. Next, a 0.6nm AlN spacer is grown, followed by a 24nm AlGaIn barrier (25% in Al content) to form the 2DEG (2-D Electron Gas) at the GaN interface, before a final 5nm in-situ SiN passivation layer is grown. Fig.1 shows a schematic of the gate stack in the MOSc-HEMT configuration. The AlGaIn barrier is removed by ICP RIE etching and GaN is recessed until depth reaches 35nm to cut the 2DEG. Finally, a 30nm ALD  $\text{Al}_2\text{O}_3$  gate oxide is deposited on the etched cavity. TEM cross section (Fig.1) illustrates the full recess configuration where sidewalls are now a part of the electron conduction path under the gate.

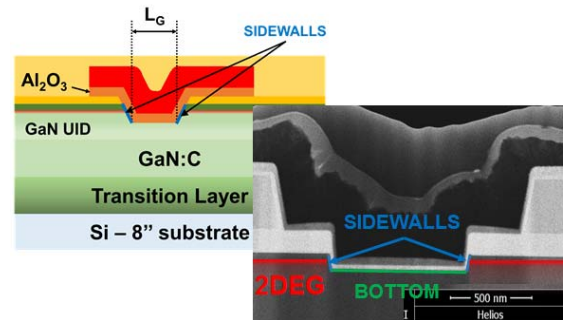


Figure 1. Schematic of the GaN-on-Si E-mode MOSc-HEMT gate stack and TEM cross section of a  $0.5 \mu\text{m}$  long recessed gate.

The nominal width of the tested devices is set at  $100\mu\text{m}$  to limit the measured current to  $10\text{mA}$  with  $L_{\text{GD}} = 15\mu\text{m}$ ,  $L_{\text{GS}} = 2\mu\text{m}$ . Fig. 2 demonstrates the E-mode ( $V_{\text{th}} > 0\text{V}$ ) operation for different gate length from  $L_{\text{G}} = 2\mu\text{m}$  down to  $0.5\mu\text{m}$ .  $V_{\text{th}}$  is extracted at a fixed current level of  $I_{\text{D}} = 10^{-5}\text{ A/mm}$ .

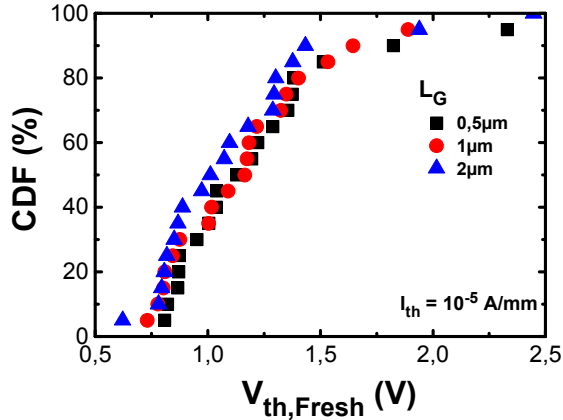


Figure 2. Cumulative distribution function of  $V_{\text{th}}$  for different  $L_{\text{G}}$  ( $0.5$ ,  $1$  and  $2\mu\text{m}$ ) confirming the E-mode operation ( $V_{\text{th}} > 0\text{V}$ ). Drain voltage is set at  $V_{\text{D}} = 0.1\text{V}$ .

### B. Experimental setup

The principle of the fast pBTI technique under AC stress is highlighted in Fig.3 and is similar to the one used for [13]. A Keysight B1500 with ultrafast SMUs (B1530) is used to pulse the gate down to  $100\text{ns}$  between two  $V_{\text{G}}$  values ( $0\text{V}$  for low state and  $+4\text{V}$  to  $+8\text{V}$  for high state). pBTI stress is applied at a given frequency ( $f = 100\text{Hz}$  to  $1\text{MHz}$ ) with a defined duty factor ( $\text{DF} = 1\%$  to  $99\%$ ) at a fixed  $V_{\text{G,Stress}}$ . A fast  $I_{\text{D}}(V_{\text{G}})$  ( $< 10\mu\text{s}$ ) is performed to record the  $\Delta V_{\text{th}}$  during the stress phase while minimizing the  $V_{\text{th}}$  recovery during a measurement phase. Consequently  $V_{\text{th}}$  recovery is measured with the same fast  $V_{\text{G}}$  ramp from  $1\mu\text{s}$  to  $100\text{s}$  at  $V_{\text{G}} = 0\text{V}$ . Note that  $V_{\text{D}} = 0\text{V}$  during stress & recovery phases while is fixed at  $0.1\text{V}$  during fast  $I_{\text{D}}(V_{\text{G}})$  measurements. From the pattern in Fig.3, it is possible to study  $\Delta V_{\text{th}}$  drift as a function of DF, frequency or total stress time ( $t_{\text{Stress,max}}$ ).

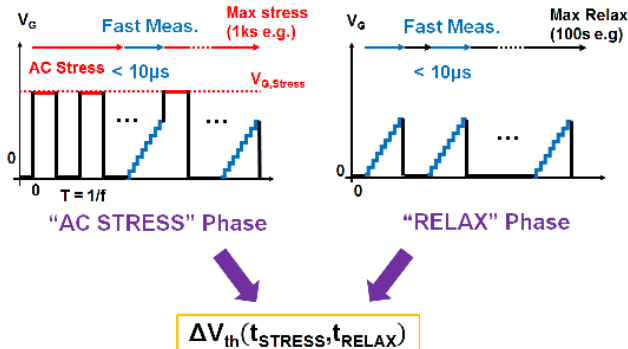


Figure 3. Principle of the AC pBTI measurement with ultra-fast  $V_{\text{th}}$  measurements minimizing unwanted  $V_{\text{th}}$  relaxation during the stress.

Fig.4 illustrates the influence of the  $I_{\text{D}}(V_{\text{G}})$  measurement time during a pBTI stress sequence. If the measurement is not fast enough ( $> 10\mu\text{s}$ ), unwanted relaxation can occur and

consequently minimize the actual  $V_{\text{th}}$  drift in the device. This would lead to misinterpretations, especially for Time to Failure (TTF) extrapolation. Measurement time has been limited to  $10\mu\text{s}$  in this study to minimize this effect.

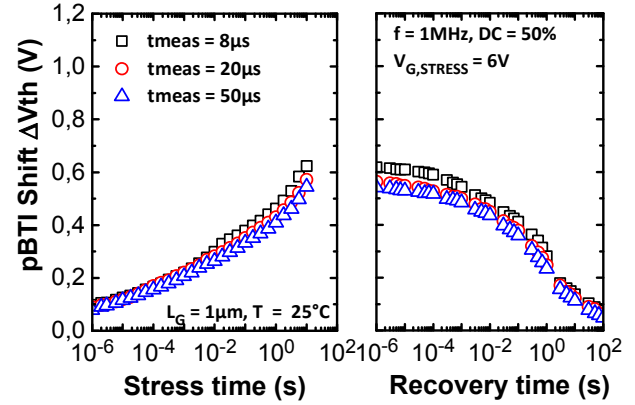


Figure 4. AC pBTI stress and recovery characteristics as a function of the  $I_{\text{D}}(V_{\text{G}})$  measurement time.  $L_{\text{G}} = 1\mu\text{m}$  and  $T = 25^\circ\text{C}$  for this measurement.

### III. DC VERSUS AC STRESS PBTI

Fig. 5 shows the pBTI stress and recovery transients for  $f = 100\text{Hz}$  to  $1\text{MHz}$  at  $\text{DF} = 50\%$  and  $V_{\text{G,Stress}} = 7\text{V}$  compared to the DC stress case. A very large difference is observed comparing AC and DC stress, furthermore the  $\Delta V_{\text{th}}$  tends to increase with the frequency of the AC signal as already reported in Si CMOS technologies [13]. This dependence is related to the fact that the AC gate signal ends up with a low state ( $V_{\text{G}} = 0\text{V}$ ) which enables the relaxation of defects compared to DC stress. This frequency effect will limit the actual  $V_{\text{th}}$  drift in GaN power transistor operating for instance at  $100\text{kHz}$ . Shape of the degradation AC pBTI shift is not monotonous and exhibits two regimes with a transition around  $t_{\text{Stress}} = 4\text{-}5\text{s}$  which might be related to multiple oxide trap populations.

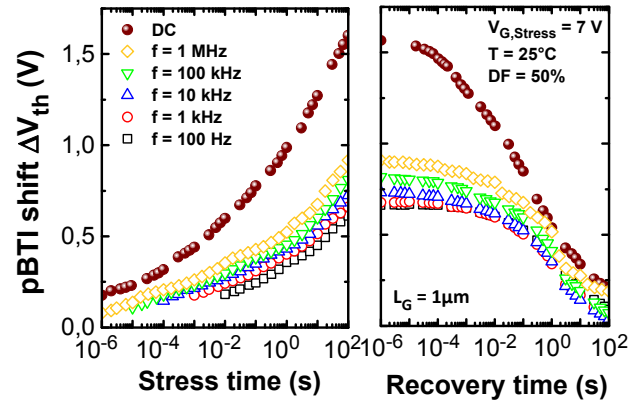


Figure 5. AC pBTI stress and recovery characteristics as a function of the signal frequency at  $\text{DF} = 50\%$ . Filled symbols represent the DC pBTI case.  $L_{\text{G}} = 1\mu\text{m}$  and  $T = 25^\circ\text{C}$  for this measurement.

The duty factor  $\text{DF}$  also modifies the  $V_{\text{th}}$  drift (See Fig. 6 plotted at a stress time of  $100\text{s}$  under  $10\text{kHz}$  AC stress). The S-curve behavior predicted by [15] is also found for our devices. Nevertheless, the global behavior differs from Si technologies where AC/DC  $V_{\text{th}}$  ratio tends to “0” for very low duty factor ( $< 1\%$ ) and to “1” for high duty factor ( $> 99\%$ ). Low DF induces

a significant degradation compared to DC case ( $\sim 0.25$ ) meaning that very fast capturing and slowly emitting traps are present in the devices ( $\tau_c/\tau_e \ll 1$ ) for capturing time below  $\tau_c < 10\mu s$ . Furthermore, the S-curve is centered on 0.55 for 50% DF, which accounts for a rather symmetrical defect distribution around  $\langle \tau_c \rangle = \langle \tau_e \rangle$  (DF = 50%). It is expected to gain at least a factor 2 on the  $\Delta V_{th}$  for a fixed stress time. Fig. 6 also highlight that gate length  $L_G$  has merely no influence on these normalized S-curves, implying similar traps characteristics even for short gate length.

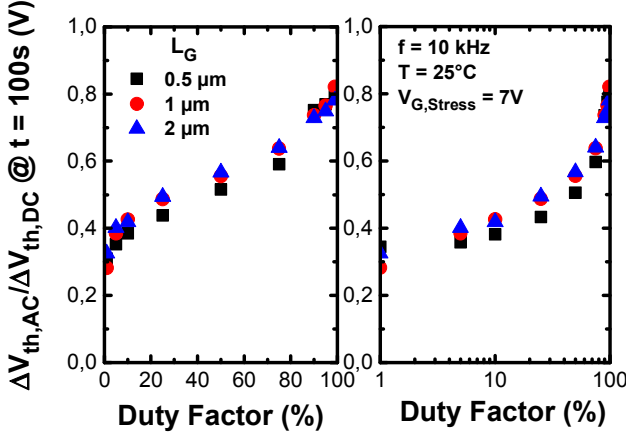


Figure 6. Variation of normalized  $\Delta V_{th,AC}/\Delta V_{th,DC}$  degradation extracted at 100s with DF. No difference with respect to gate length is observed.  $V_g = 7V$  and  $f = 10kHz$  here.

For a recoverable degradation with a single oxide trap population, BTI modeling [14] foresees  $\Delta V_{th}$  to follow the model:

$$\Delta V_{th} = C_R \cdot V_G^\gamma \cdot \exp\left(-\frac{qE_A}{k_B T}\right) \cdot \ln\left(1 + \frac{\tau_c \cdot t_S}{\tau_e \cdot t_R}\right) \quad (1)$$

where  $C_R$  is a constant,  $\gamma$  is the voltage acceleration factor,  $E_A$  is the activation energy of the oxide traps,  $\tau_c$  and  $\tau_e$  the average time constant of the oxide traps inducing a recoverable degradation. Finally,  $t_S$  and  $t_R$  represent the stress and relaxation time used in the measurement.

Thus, it is possible in the case of a single recoverable degradation, to normalize pBTI shift as a function of the  $t_S/t_R$  ratio for multiple  $t_S$  values. Figure 7 presents this approach for our  $1\mu m$  long devices under a  $V_{G,Stress} = 7V$  at  $f = 1MHz$  and DF = 50%, the redline representing the law (1). By plotting the recovery transients  $\Delta V_{th, recovery}$  as a function of the maximum stress time vs recovery time ratio ( $t_{Stress, max}/t_{recovery}$ ), we show a deviation from the analytical normalization. It suggests that our degradation is not related to single recoverable trap population but that multiple traps must be considered to understand BTI degradation in MOSc-HEMT devices.

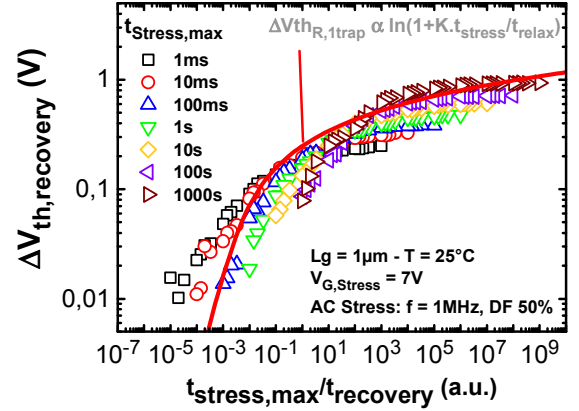


Figure 7. Recovery transients after an 1MHz AC stress plotted as a function of  $t_{Stress, MAX}/t_{recovery}$  showing no normalization, sign of multiple traps populations.  $V_{G,Stress} = 7V$  and  $L_G = 1\mu m$  here.

#### IV. AC PBTI MODELING

To understand the degradation kinetics of our gate stack, we use a “RC model” combined with a CET (Capture Emission Time) map proposed in [13,15]. Fig. 8 illustrates the principle of the RC model where the oxide traps are modeled by a RC parallel network.

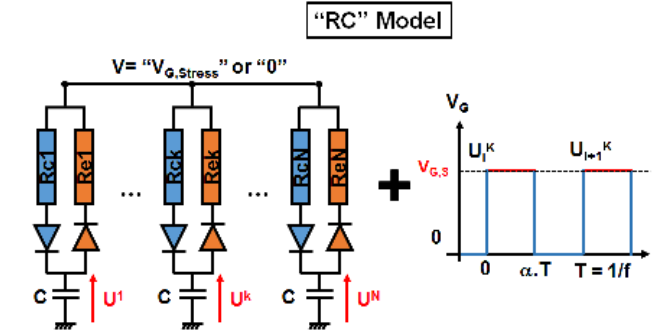


Figure 8. Schematic of the RC network used for BTI modeling [13,15]. Each traps is represented by a combination of a capacitor C and by two resistances  $R_e$  and  $R_c$  to set emission and capture time respectively. In the case of AC BTI, this circuit is studied under a  $V_g$  signal given by the chronogram (right) which gives access to the capacitor voltage  $U(t)$  after a given number of cycles.

For general AC signal ending with a relaxation phase (our case here), it is possible to have access to the voltage  $U$  after  $n$  stress cycles:

$$U_{n, low} = V_G \left[ 1 - e^{-nT \cdot \delta} \right] \cdot \frac{e^{-T \cdot \beta} - e^{-T \cdot \delta}}{1 - e^{-T \cdot \delta}} \quad (2)$$

where  $\delta = \alpha \tau_c + (1 - \alpha)/\tau_e$  and  $\beta = (1 - \alpha)/\tau_e$ .  $\alpha$  is the duty factor in this analysis.  $\tau_c$  and  $\tau_e$  the average time constant of the oxide traps while  $V_G$  is the stress voltage applied on the gate during high state AC phase.

This RC model can be combined with a “CET” (Capture Emission Time) map which represents a traps occupancy map and giving a normalized traps density  $g(\tau_c, \tau_e)$  between 0 and 1. It enables the calculation of  $\Delta V_{th}$  as a function of  $t$  by summing the filling state of each traps “i”:



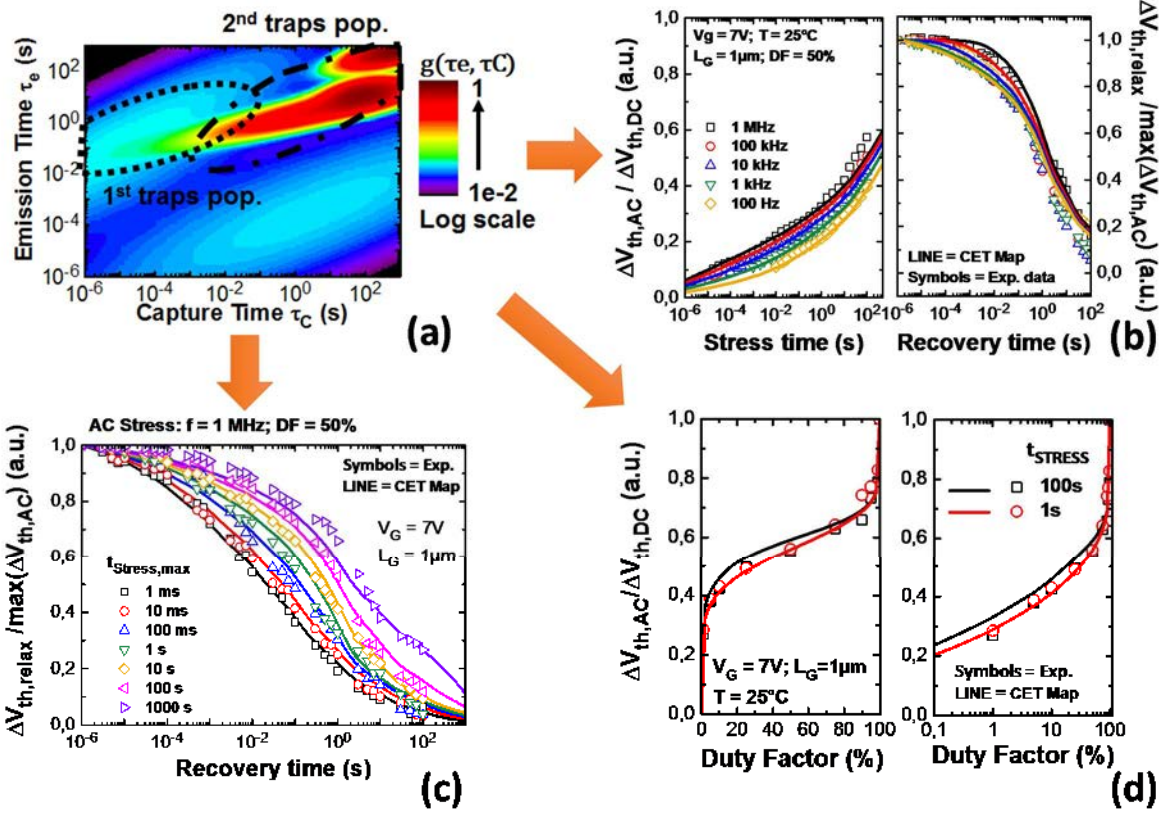


Figure 9. (a) Capture and Emission Time (CET) map giving the traps density  $g(\tau_c, \tau_e)$ . This map shows two population, one for short time degradation and a second one for long time degradation with a very specific emission time around 4-5s. Comparison of experimental and modeled  $\Delta V_{th}$  (b) stress and recovery for increasing frequencies, (c)  $\Delta V_{th}$  recovery after increasing AC stress time (1ms to 1ks) and (d)  $\Delta V_{th}$  AC/DC degradation ratio as a function of DF.

$$\Delta V_{th}(t) = K \cdot \sum_{i=1}^N g(\tau_c^i, \tau_e^i) \cdot U^i(t) \quad (3)$$

where  $K$  is a technological constant and  $\tau_e$ ,  $\tau_c$ ,  $U$  the previously defined traps parameters. The CET map used to reproduce experimental data is presented in Fig. 9. , reproduces well several features of the experimental  $\Delta V_{th}$  degradation and recovery phase for our transistors. Frequency dependence at  $DF = 50\%$  (Fig. 9.(b)) as well as  $\Delta V_{th}$  relaxation as function of total stress time (Fig. 9.(c)) under  $V_{G,Stress} = 7V$  at  $f = 1MHz$  and  $DF = 50\%$  are fitted with accuracy, providing a validation of our CET map in the case of  $\tau_e > \tau_c$ . The second part of the map ( $\tau_e < \tau_c$ ) can be assessed by fitting the AC/DC S-curves (Fig. 9.(d)) as a function of the duty factor  $DF$ , which has been done at two stress times (1s and 100s). It can be seen that two trap populations have been used to fit our data. A first one at short capture time and moderate emission time, while a second one is used to model the long term degradation and relaxation transients observed experimentally between 1 and 100s. Still, no permanent degradation were considered here because every relaxation characteristics tend to reach 0 and no permanent degradation has been observed for measurements done a week after this study (not shown here). This CET map can be used to extrapolate a degradation or a recovery time for a given  $V_G$  (here 7V). TCAD simulations were performed to estimate the

electric field distribution around the recessed MOS gate. Fig. 10 shows the simulated E-field undergone by the  $Al_2O_3$  gate oxide (30nm here) in the recess configuration cited in section II.A. The electric field modulus represented in color scale indicates a uniform distribution all along the bottom part of the gate. However, non-uniformities appear at the gate corners and sidewalls, which would potentially lead to a different  $V_{th}$  degradation in these regions.

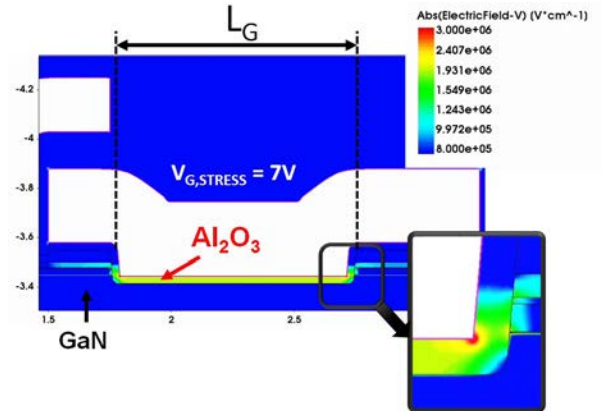


Figure 10. TCAD simulation of electric field distribution under  $V_{G,Stress} = 7V$  on 30nm  $Al_2O_3$ /GaN MOS gate stack including gate field plate and GaN-UID recess introduced in section II-A. Gate length is set at  $L_G = 1\mu m$  here. Whiteout areas are related to metallic materials.

It has to be noted that these TCAD simulations do not embed the evaluation of interface traps which would be different in the sidewalls compared to the bottom of the etched cavity and thus imply a different  $V_{th}$  in these two regions.

This CET methodology provides a precise tool to deeply understand the degradation of our gate oxide in the case of fully recessed MOS gate where some fast degradations can occur and how the device would behave in AC mode which represents the actual operation when integrated into applications. Here the CET map has been evaluated at a given  $V_{G,Stress} = 7V$  but must be reconsidered, or at least checked, when stress voltage is modified. Of course this approach does not take into account the  $\Delta V_{th}$  induced by an OFF state stress ( $V_{G,OFF} = 0V$ ;  $V_{D,OFF} > 600V$ ) and should be tested afterwards.

## V. ACCELERATION FACTORS

The previous section allows us to revisit results established for standard DC stress. Besides, the classical voltage and temperature dependence have to be readapted in the case of GaN MOSc-HEMT technology. The voltage acceleration factor  $\gamma$  (see (1)) has been extracted for a  $1\mu m$  gate length transistor at different stress times (1ms, 1s and 100s) under a 100kHz AC stress (DF = 50%) (see Fig. 11-left). Generally constant for high reliability CMOS technology, this factor varies here as a function of the stress time which clearly shows the two trap populations are not filled identically with  $V_G$  and that the CET map is not unique (to be recalculated for each  $V_{G,Stress}$ ). Short capture time traps are more easily filled when  $V_G$  increases while the long capture time traps tend to be less sensitive to  $V_G$ . The activation energy of the  $\Delta V_{th}$  drift has been extracted (Fig. 11-right) and shows a constant value around  $E_a = 85meV$  as a function of the stress time, indicating that the 1<sup>st</sup> trap population of the CET map tends to governs the temperature dependence of the degradation.

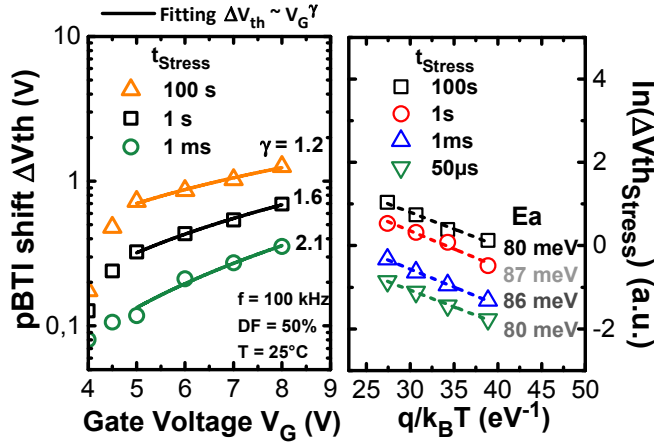


Figure 11. Voltage acceleration factor evaluation under AC stress (left) and activation energy extraction (right) extracted on MOSc-HEMT technology. Frequency is set at 100kHz to be close to operating conditions.

Time to Failure (TTF) is presented on Fig.12 for two criteria on  $\Delta V_{th}$  (0.3 and 0.75V) as a function of  $V_G$  for DC and AC stress ( $f = 100kHz$ , DF = 50%). It is pointed out that two different  $V_G$  dependence exist following the criteria. This latter

effect can be related to the variation of  $\gamma$  with stress time (Fig. 11-left) because low  $\Delta V_{th}$  is achieved in the first regime of the  $V_{th}$  degradation spectrum, i.e. at low stress time as thus related to a high acceleration factor, whereas high  $\Delta V_{th}$  criteria is associated with the second regime that appears for stress time  $> 4-5s$  (see Fig. 5) which is correlated to lower  $\gamma$ . Meanwhile, for large  $V_{G,Stress}$  the TTF is considerably extended when HEMTs undergo an AC gate pattern. Plus, at low  $V_G$ , TTF tends to diverge from the standard DC power law (eq. (1)), which is consistent with the drop of  $\gamma$  observed at low voltage ( $V_{G,Stress} < 5V$ ) on Fig.11-left.

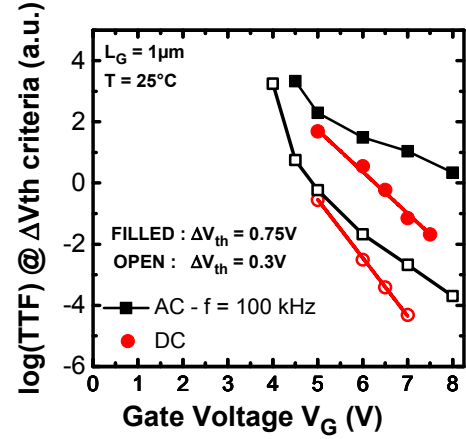


Figure 12. Time to Failure versus gate voltage at two criteria (0.3 and 0.75V) emphasizing the gain in lifetime under AC stress conditions.

## VI. DYNAMIC VARIABILITY

Dynamic variability has also been studied (Fig. 13 & 14) at wafer level. Fig. 13 depicts that  $\Delta V_{th}$  follows a normal law generally expected for large area devices (Probability Distribution Function is a Gaussian in this case) and that standard deviation for  $\Delta V_{th}$  distribution increases all along the AC stress phase.

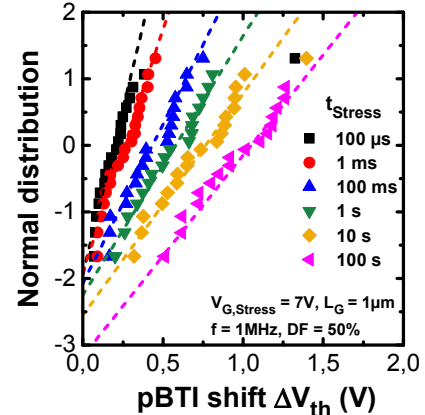


Figure 13.  $\Delta V_{th}$  distributions after increasing stress time. Normal law catches the behavior.  $V_G = 7V$  and  $L_G = 1\mu m$  here.

This feature is in agreement with a Poisson defect distribution in the gate oxide. Gate length influence on  $\Delta V_{th}$  distributions is presented on Fig. 14 extracted after 100 $\mu s$  and 100s of AC stress ( $V_{G,Stress} = 7V$ ,  $f = 1MHz$  and DF = 50%). Hardly no

difference between  $L_G = 0.5$  and  $1\mu\text{m}$  is observed which means that defect distribution is basically the same for both gate length. For  $L_G = 2\mu\text{m}$  on the opposite, a slight increase of the dynamic variability is observed, potentially due to a lower initial  $V_{th}$  distribution, which increases the gate overdrive  $V_{G,ov} = V_{G,Stress} - V_{th}$  and so the value of the electric field during the stress.

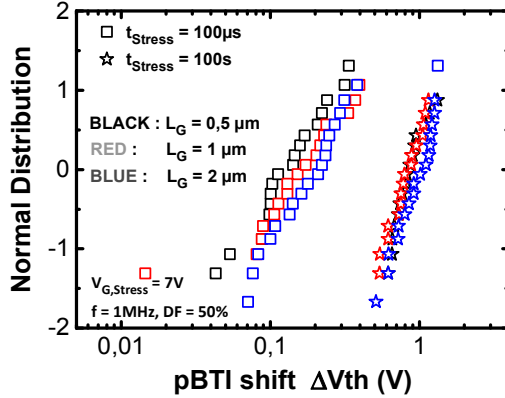


Figure 14.  $\Delta V_{th}$  distributions after two stress times (100 $\mu\text{s}$  and 100s). No visible difference is observed between 0.5 and  $1\mu\text{m}$  gate length.  $f = 1\text{MHz}$  and  $V_{G,Stress} = 7\text{V}$  here.

The strong standard deviation observed of the normal distributions used to fit experimental data indicates that this gate configuration must be optimized, whether in terms of material defectivity or through gate recessing uniformity all over the wafer. This is a key point to qualify the MOSc-HEMT technology for power applications, and to improve gate reliability of these promising devices.

## CONCLUSIONS

A novel insight of the pBTI degradation of GaN power transistors has been presented allowing to assess the  $\Delta V_{th}$  shift during the actual operation of the device through AC stress phase and ultra-fast  $I_D(V_G)$  characterization. CET map combined with an RC model enables to deeply understand the degradation kinetics of our devices. This methodology has been applied for the first time on E-mode GaN-on-Si MOSc-HEMT showing the presence of two trap populations in the oxide of the tested devices. Acceleration factors (voltage, temperature) have been extracted and tend to confirm the two degradation regimes. The Time to Failure is improved in the case of AC stress compared to DC stress implying an underestimation of this parameter in DC pBTI studies. The methodology presented in this paper has to be considered for the qualification of the MOS-c HEMT configuration and extended to assess the  $V_{th}$  degradation kinetics under harsh OFF state conditions (high  $V_{DS}$ ,  $V_G = 0\text{V}$ ).

- [1] P. Moens, C. Liu, A. Banerjee, P. Vanmeerbeek, P. Coppens, H. Ziad et al., "An industrial process for 650V rated GaN-on-Si power devices using in-situ SiN as a gate dielectric," in *Proc. 2014 IEEE 26th Power Semiconductor Devices & IC's (ISPSD) Conf.*, pp. 374-377.
- [2] S. Kaneko, M. Kuroda, M. Yanagihara, A. Ikoshi, H. Okita, T. Morita et al., "Current-collapse-free operations up to 850 V by GaN-GIT utilizing hole injection from drain," in *Proc. 2015 IEEE 27th Power Semiconductor Devices & IC's (ISPSD) Conf.*, pp. 41-44.
- [3] P. Moens, M.J. Uren, A. Banerjee, M. Meneghini, B. Padmanabhan, W. Jeon et al., "Current-collapse-free operations up to 850 V by GaN-GIT utilizing hole injection from drain," in *Proc. 2017 IEEE 29th Power Semiconductor Devices & IC's (ISPSD) Conf.*, pp. 97-100.
- [4] M. Meneghini, I. Rossetto, M. Borgia, E. Canato, C. De Santi, F. Rampazzo et al., "Degradation of GaN-HEMTs with p-GaN Gate: Dependence on temperature and on geometry," in *Proc. 2017 IEEE 56th International Reliability Physics Symposium (IRPS) Conf.*, pp. 4B-5.1-4B-5.5.
- [5] S. Stoffels, B. Bakeroot, T.L. Wu, D. Marcon, N.E. Posthuma, S. Decoutere et al., "Failure mode for p-GaN gates under forward gate stress with varying Mg concentration," in *Proc. 2017 IEEE 56th International Reliability Physics Symposium (IRPS) Conf.*, pp. 4B-4.1-4B-4.9.
- [6] M. Meneghini, I. Rossetto, D. Bisi, M. Ruzzarin, M. Van Hove, S. Stoffels et al., "Negative bias-induced threshold voltage instability in GaN-on-Si power HEMTs," *IEEE Elec. Dev. Lett. vol. 37 (4)*, pp. 474-477, Apr. 2016.
- [7] G.P. Lansbergen, K.Y. Wong, Y.S. Lin, J.L. Yu, F.J. Yang, C.L. Tsai et al., "Threshold voltage drift (PBTI) in GaN D-MODE MISHEMTs: Characterization of fast trapping components," in *Proc. 2014 IEEE 56th International Reliability Physics Symposium (IRPS) Conf.*, pp. 6C.4.1-6C.4.6.
- [8] P. Lager, C. Ostermaier, G. Pobegenand and D. Pogany, "Towards Understanding the Origin of Threshold Voltage Instability of AlGaN/GaN MIS-HEMTs" in *Proc. 2012 IEEE International Electron Devices Meeting (IEDM) Conf.*, pp. 12.299-12.302.
- [9] T.L. Wu, J. Franco, D. Marcon, B. De Jaeger, B. Bakeroot, X. Kang et al., "Positive bias temperature instability evaluation in fully recessed gate GaN MIS-FETs" in *Proc. 2016 IEEE 55th International Reliability Physics Symposium (IRPS) Conf.*, pp. 4A21-4A26.
- [10] L. Di Cioccio, E. Morvan, M. Charles, P. Perichon, A. Torres, F. Ayel et al., "From epitaxy to converters topologies what issues for 200 mm GaN/Si?" in *Proc. 2015 IEEE International Electron Devices Meeting (IEDM) Conf.*, pp. 16.5.1-16.5.4.
- [11] M. Hua, Z. Zhang, J. Wei, J. Lei, G. Tang, K. Fu et al., "Integration of LPCVD-SiNx gate dielectric with recessed-gate E-mode GaN MIS-FETs: Toward high performance, high stability and long TDDB lifetime," in *Proc. 2016 IEEE International Electron Devices Meeting (IEDM) Conf.*, pp. 10.4.1-10.4.4.
- [12] E. Acurio, F. Crupi, P. Magnone, L. Trojman and F. Iucolano, "Impact of AlN layer sandwiched between the GaN and the Al2O3 layers on the performance and reliability of recessed AlGaN/GaN MOS-HEMTs," *Microelec. Engineer., vol. 178*, pp. 42-47, June 2017.
- [13] A. Subirats, X. Garros, J. Cluzel, J. El Husseini, F. Cacho, X. Federspiel et al., "A new gate pattern measurement for evaluating the BTI degradation in circuit conditions" in *Proc. 2017 IEEE 56th International Reliability Physics Symposium (IRPS) Conf.*, pp. 5D.1.1-5D.1.5.
- [14] V. Huard, C. Parthasarathy, N. Rallet, C. Guerin, M. Mammase, D. Barge et al., "New characterization and modeling approach for NBTI degradation from transistor to product level" in *Proc. 2007 IEEE International Electron Devices Meeting (IEDM) Conf.*, pp. 797-800.
- [15] H. Reisinger, T. Grasser, K. Ermisch, H. Nielen, W. Gustin and C. Schlunder, "Understanding and modeling AC BTI" in *Proc. 2017 IEEE 56th International Reliability Physics Symposium (IRPS) Conf.*, pp. 5D.1.1-5D.1.5.